

Analytic Detection Thresholds for Measurements of Linearly Polarized Intensity Using Rotation Measure Synthesis

C. A. Hales^{1,2*}, B. M. Gaensler^{1,3}, R. P. Norris² and E. Middelberg⁴

¹*Sydney Institute for Astronomy, School of Physics, The University of Sydney, NSW 2006, Australia*

²*CSIRO Astronomy & Space Science, PO Box 76, Epping, NSW 1710, Australia*

³*Australian Laureate Fellow*

⁴*Astronomisches Institut, Ruhr-Universität Bochum, Universitätsstr. 150, 44801 Bochum, Germany*

27 August 2018

ABSTRACT

A fully analytic statistical formalism does not yet exist to describe radio-wavelength measurements of linearly polarized intensity that are produced using rotation measure synthesis. In this work we extend the analytic formalism for standard linear polarization, namely that describing measurements of the quadrature sum of Stokes Q and U intensities, to the rotation measure synthesis environment. We derive the probability density function and expectation value for Faraday-space polarization measurements for both the case where true underlying polarized emission is present within unresolved Faraday components, and for the limiting case where no such emission is present. We then derive relationships to quantify the statistical significance of linear polarization measurements in terms of standard Gaussian statistics. The formalism developed in this work will be useful for setting signal-to-noise ratio detection thresholds for measurements of linear polarization, for the analysis of polarized sources potentially exhibiting multiple Faraday components, and for the development of polarization de-biasing schemes.

Key words: methods: analytical, statistical — radio continuum: general — radio lines: general — techniques: polarimetric.

1 INTRODUCTION

Radio-wavelength observations of linearly polarized synchrotron emission enable studies of ionized gas and magnetic fields in, and along the lines-of-sight to, energetic astrophysical environments. Faraday rotation measure (RM) synthesis (Burn 1966; Brentjens & de Bruyn 2005) is a technique for Fourier transforming observational polarimetric data to produce a complex Faraday dispersion spectrum. The magnitude of this spectrum, which we denote by $|\mathcal{F}(\alpha, \delta, \phi)|$, encapsulates the intensity of linearly polarized emission exhibited at different Faraday depths¹, ϕ , along a single physical line of sight with sky coordinate (α, δ) .

Statistics describing measurements of linearly polarized intensity derived from $|\mathcal{F}(\alpha, \delta, \phi)|$ have been investigated empirically by George et al. (2011) and analytically

by Macquart et al. (2012). However, a fully analytic description is yet to be presented. Such statistics are required to enable detailed quantitative analysis of polarimetric data from existent radio facilities such as the Australia Telescope Compact Array Broadband Backend (Wilson et al. 2011), the Westerbork Synthesis Radio Telescope, the Giant Metrewave Radio Telescope, and the Expanded Very Large Array (Perley et al. 2011), and from future surveys such as POSSUM (Gaensler et al. 2010) with the ASKAP observatory (Johnston et al. 2008; Deboer et al. 2009), GALFACTS (Taylor & Salter 2010) with the Arecibo observatory, and the Magnetism Key Science Project² with the Low Frequency Array.

The statistics exhibited by Faraday-space measurements of linear polarization are qualitatively similar, yet in general quantitatively different, to those of standard linear polarization. Intensity measurements of the latter, denoted³

* E-mail: c.hales@physics.usyd.edu.au

¹ Faraday depth is not a physical depth, but rather the depth of Faraday rotating magnetised plasma between a source of polarized emission and the telescope; see equation (3) from Brentjens & de Bruyn (2005).

² <http://www.mpifr-bonn.mpg.de/staff/rbeck/MKSP/mksp.html>

³ The term L is commonly used to differentiate linear polarization from the more general elliptical polarization $P \equiv$

by L , are obtained for a given line of sight by taking the quadrature sum of measured Stokes Q and U intensities, namely

$$L(\alpha, \delta) \equiv \sqrt{[Q(\alpha, \delta)]^2 + [U(\alpha, \delta)]^2}. \quad (1)$$

The statistics of L and discussion of detection thresholds are well documented (Rice 1945; Simmons & Stewart 1985; Leahy & Fernini 1989; Vaillancourt 2006). In contrast, intensity measurements of Faraday-space linear polarization must be obtained by first devising a method to extract some, or all, of the polarized emission that may be present over a range of Faraday depths (ϕ) within the Faraday dispersion spectrum (\mathcal{F}) for a given line of sight. The specifics of this extraction process will dictate the resulting polarization measurement statistics. In this work we focus on measurements produced by extracting the peak⁴ intensity from a cleaned (Heald et al. 2009) Faraday dispersion spectrum, denoted by \mathcal{F}^{cln} (note that this is not the clean component spectrum, but rather the cleaned spectrum which contains convolved clean components plus residuals), namely

$$L_{RM}(\alpha, \delta) \equiv \max \left(|\mathcal{F}^{cln}(\alpha, \delta, \phi)| \right), \quad (2)$$

where we use the term L_{RM} to differentiate these measurements from those of standard L . Measurements of L_{RM} , as defined in equation (2), are suitable for the analysis of data consisting of unresolved⁵ polarized emission in Faraday space; such conditions are often encountered observationally due to the limited bandwidth capabilities of many present-day telescopes (e.g. Heald et al. 2009) or the underlying physics of target sources (e.g. pulsars). Like L , L_{RM} is positive semi-definite (≥ 0) and exhibits non-Gaussian statistics.

In this paper we seek to relate the statistical significance of measurements of L_{RM} with those of L and of standard Gaussian statistics for general observational setups, in order to facilitate detailed quantitative analysis. To meet this aim we analytically, rather than empirically, derive the probability density function (PDF) and expectation value for measurements of L_{RM} for the general case where true underlying polarized emission is present, and for the limiting case where no such emission is present. For comparison, we note that George et al. (2011) have presented an empirical investigation of detection thresholds and the PDF for L_{RM} for a specific observational setup; we seek to formally

$\sqrt{Q^2 + U^2 + V^2}$, which includes Stokes V . While we do not use P in this work, we follow the L notation to ensure consistency with future deep surveys in which many sources exhibiting both L and P emission are likely to be detected.

⁴ In practice, the peak should be fitted to minimise pixel discretisation errors; for example, see discussion of 3-point parabolic fits by Hales et al. (2012).

⁵ Just as the peak surface brightness of an unresolved source in a two-dimensional (2D) image (measured in Jy beam⁻¹) is equal in magnitude to its integrated surface brightness (or flux density; measured in Jy), so too is the peak polarized intensity of an unresolved component in Faraday space (measured in Jy beam⁻¹ RMSF⁻¹, where RMSF is the rotation measure spread function, or the unit of resolution in Faraday space; Brentjens & de Bruyn 2005) equal in magnitude to its Faraday-integrated polarized intensity (measured in Jy beam⁻¹), modulo any statistical or measurement-induced biases.

generalise these results here. Additionally, through comparison with simulated data, Macquart et al. (2012) identified a missing correction factor in their analytic PDF that we derive here.

We begin in § 2 by reviewing the existing analytic statistical description of L , and by deriving a relationship that equates the significance of detections in L with those of Gaussian statistics. In § 3 we extend these analytic results to L_{RM} , noting two key experiment-specific parameters that dictate its observed statistical properties. In § 4 we demonstrate use of our derived significance relationships for L and L_{RM} through worked examples, and discuss how individual lines of sight exhibiting multiple unresolved Faraday-space components may be treated. In § 5 we use our analytic results to illustrate how cross-sectional profiles for astronomical sources with 2D elliptical Gaussian morphologies are affected when observed in images exhibiting polarization measurement statistics, namely, where each pixel in an image of L or L_{RM} is formed using equation (1) or (2), respectively. Using these profiles we briefly outline challenges for robust source extraction in polarization images. In § 6 we address the point recently raised by George et al. (2011) that non-Gaussianities in images of Stokes Q and U will complicate the calculation of robust significance relationships. We present our conclusions and comment on future work regarding polarization bias in § 7.

For notational convenience throughout this work we will drop the explicit (α, δ) notation (cf. equations above), but note that the statistics we discuss refer to the distribution of intensities that an individual line of sight (or pixel) may exhibit. As pointed out in § 2, this is not necessarily the same as discussing the statistics of a sample of measurements from different lines of sight, or pixel intensities within some spatial region of an image.

2 STANDARD LINEAR POLARIZATION

The magnitude of observed standard linear polarization, L , is given by equation (1). For true underlying Stokes intensities Q_0 and U_0 in the presence of Gaussian measurement errors σ_Q and σ_U , respectively, the observed Stokes intensities Q and U as used in equation (1) are given by

$$Q = Q_0 \pm \sigma_Q, \quad (3)$$

$$U = U_0 \pm \sigma_U. \quad (4)$$

The true underlying and unbiased linearly polarized signal is given by

$$L_0 = \sqrt{Q_0^2 + U_0^2}. \quad (5)$$

Measurements of Stokes Q and U may be obtained at radio wavelengths using either individual spectral channel observations, resulting in individual measurements of L for each observed channel, or band-averaged (e.g. using multi-frequency synthesis) observations, resulting in a single measurement of L for the entire band. Analytically, there is no need to differentiate between these two approaches; the analytic statistical descriptions of L for the individual channel and band-averaged approaches are identical; both can be described by equations (3) and (4) for a sample of measurements with given L_0 . For completeness, we note that

the technique of RM-synthesis is preferable to the band-averaged L approach because the latter is more prone to bandwidth depolarization, in which rotations of spectral Q and U measurements through the complex plane can cause their band-averaged values to become diminished. Separately, we note that discussion regarding the statistics of stacked measurements of L is beyond the scope of this work; for example, as a result of summing multiple L measurements from individual spectral channels over which Faraday rotation may be occurring.

The PDF for L is given by Rice (1945) as

$$f(L|L_0) = \frac{L}{\sigma_{Q,U}^2} \exp\left(-\frac{L^2 + L_0^2}{2\sigma_{Q,U}^2}\right) I_0\left(\frac{LL_0}{\sigma_{Q,U}^2}\right), \quad (6)$$

where $\sigma_{Q,U}$ is a noise term explained below, $L \geq 0$, $I_k(x)$ is a modified Bessel function of the first kind with order k and argument x , and it is assumed that the true polarized intensity L_0 (≥ 0) is known. In equation (6) and in future use, we simplify notation by assuming that measurement error is implicitly specified in all priors; for example, we imply $f(L|L_0) \equiv f(L|L_0, \sigma_{Q,U})$. Equation (6) is known as the Ricean distribution. Formally, it is only valid for $\sigma_{Q,U} = \sigma_Q = \sigma_U$. We assume this to be the case here, and discuss issues regarding $\sigma_Q \neq \sigma_U$ in Appendix A. The Ricean distribution is displayed for several values of the ratio $L_0/\sigma_{Q,U}$ in the top panel of Fig. 1.

The cumulative distribution function (CDF) for L is obtained by integrating equation (6), giving

$$F(L|L_0) = 1 - \mathcal{Q}_1\left(\frac{L_0}{\sigma_{Q,U}}, \frac{L}{\sigma_{Q,U}}\right), \quad (7)$$

where $\mathcal{Q}_1(\alpha, \beta)$ is the Marcum Q-function (Marcum 1948). $\mathcal{Q}_1(\alpha, \beta)$ is defined by

$$\mathcal{Q}_1(\alpha, \beta) = \int_{\beta}^{\infty} x \exp\left(-\frac{x^2 + \alpha^2}{2}\right) I_0(\alpha x) dx, \quad (8)$$

and may be efficiently calculated using the algorithm presented by Simon (1998).

Rice (1945) gives both the expectation value (E) and variance (Var) of equation (6) as

$$E(L|L_0) = \sqrt{\frac{\pi\sigma_{Q,U}^2}{2}} {}_1F_1\left(-\frac{1}{2}; 1; -\frac{L_0^2}{2\sigma_{Q,U}^2}\right), \text{ and} \quad (9)$$

$$\text{Var}(L|L_0) = L_0^2 + 2\sigma_{Q,U}^2 - [E(L|L_0)]^2, \quad (10)$$

where ${}_1F_1$ is a confluent hypergeometric function. In the absence of input signal (i.e. $L_0 = 0$), the Ricean distribution limits to the Rayleigh (1880) distribution given by

$$f(L|L_0 = 0) = \frac{L}{\sigma_{Q,U}^2} \exp\left(-\frac{L^2}{2\sigma_{Q,U}^2}\right), \quad (11)$$

where $L \geq 0$. The expectation value and variance of the Rayleigh distribution is given by

$$E(L|L_0 = 0) = \sqrt{\frac{\pi\sigma_{Q,U}^2}{2}}, \text{ and} \quad (12)$$

$$\text{Var}(L|L_0 = 0) = (4 - \pi)\frac{\sigma_{Q,U}^2}{2}. \quad (13)$$

The CDF for the Rayleigh distribution is obtained by integrating equation (11), giving

$$F(L|L_0 = 0) = 1 - \exp\left(-\frac{L^2}{2\sigma_{Q,U}^2}\right). \quad (14)$$

Unlike a Gaussian distribution, the Ricean distribution is signal (i.e. L_0) dependent; the Ricean PDF changes shape depending on the magnitude of the underlying input signal (in comparison, the shape of a Gaussian distribution is not influenced by terms in its PDF that relate to its true or observed mean). The Ricean distribution is positively skewed (right-skewed) and leptokurtic (positive excess kurtosis) for weak input signal, while for stronger input signal the distribution becomes Gaussian about mean L_0 with standard deviation $\sigma_{Q,U}$. It is this signal dependence that prevents one from assuming a uniform variance (i.e. from assuming that $\text{Var}(L|L_0)$ from equation (10) is uniform) for different lines of sight that have equal $\sigma_{Q,U}$ (for example, a sample of spatial pixels with equal $\sigma_{Q,U}$ in an image of L , where the intensity for each pixel is calculated using equation (1)). The signal dependence also complicates estimation of L_0 given a measurement of L (e.g. Simmons & Stewart 1985; Leahy & Fernini 1989; Vaillancourt 2006).

We note that while the PDF for L is non-Gaussian, the *noise* in a Ricean distribution (represented by $\sigma_{Q,U}$) is Gaussian in character, reflecting the nature of measurement uncertainty in Stokes Q and U (such that $\sigma_{Q,U}$ characterises the manner in which random errors are propagated into measurements of L). The term *Ricean noise* therefore has the potential to be misleading, as it may incorrectly suggest that the Ricean distribution exhibits those properties usually associated with regular Gaussian noise, such as signal-independence. If the term Ricean noise is used, then the prefix *Ricean* should be interpreted in the same way that, for example, *shot* noise, which is governed by Poissonian statistics and is thus signal-dependent, differentiates itself from standard Gaussian noise.

2.1 Detection Significance

To quantify the significance of a measurement of L in terms of a well-recognised statistic, we relate its probability for Type I (false positive) error to that of an equivalent measurement of intensity in Gaussian noise. We use the term “equivalent” to indicate that the same noise term $\sigma_{Q,U}$ from L is used as the standard deviation for the Gaussian distribution. We define the signal-to-noise ratio (SNR) of a measurement of L as $L/\sigma_{Q,U}$. This definition makes use of the observable quantities L and $\sigma_{Q,U}$; we do not relate L to equation (10), which includes the unobservable and L_0 -dependent term $E(L|L_0)$. We generically denote a measurement of intensity in Gaussian noise by G (e.g. a measurement of Stokes Q intensity), and define the SNR of our equivalent Gaussian measurement as $G/\sigma_{Q,U}$. By equating the CDF for a Rayleigh distribution [equation (14)] with the standard confidence interval for a Gaussian (i.e. $\text{erf}[|G|/(\sqrt{2}\sigma_{Q,U})]$, not its CDF), and by selecting the magnitude of G as the appropriate equivalent measure to compare with L , we quantify the Gaussian equivalent significance, denoted by G^{ES} , for a measurement of L as

$$|G^{ES}|/\sigma_{Q,U} \equiv \sqrt{2} \text{erf}^{-1}\left\{1 - \exp\left[-\frac{1}{2}\left(\frac{L}{\sigma_{Q,U}}\right)^2\right]\right\}, \quad (15)$$

or, conversely, the linear polarization equivalent significance, denoted by L^{ES} , for a measurement of G as

$$L^{ES}/\sigma_{Q,U} \equiv \sqrt{-2 \ln \left[1 - \operatorname{erf} \left(\frac{1}{\sqrt{2}} \frac{|G|}{\sigma_{Q,U}} \right) \right]}, \quad (16)$$

where erf and erf^{-1} are the error function and its inverse, respectively.

The Gaussian equivalent significance relationships above may be used to set SNR cutoffs for polarization surveys, designed to meet the same statistical criteria as standard G/σ SNR cutoffs in surveys with Gaussian noise. Examples illustrating use of these equations are presented in § 4. Equation (16), and thus implicitly equation (15), is displayed in Fig. 2.

3 FARADAY-SPACE LINEAR POLARIZATION

In this section we derive customised statistics to describe measurements of L_{RM} obtained using equation (2). We begin by discussing two experiment-specific parameters that will be needed for this derivation: M , which characterises an effective sample size in Faraday space, and σ_{RM} , which characterises the noise in L_{RM} .

RM-synthesis can be thought of as a technique to evaluate $\mathcal{F}(\phi)$ over a range of trial Faraday depths spanning $\pm\phi_{max}$, which may be set by [equations (35) and (63) from Brentjens & de Bruyn 2005]

$$\phi_{max} \approx \frac{\sqrt{3}}{\min[\delta(\lambda_i^2)]}, \quad (17)$$

where $\delta(\lambda_i^2)$ are spectral channel widths in wavelength-squared (λ^2) space for each i 'th observed channel; the minimum $\delta(\lambda_i^2)$ characterises the maximum Faraday depth ϕ_{max} at which polarized emission can be detected. The effective resolution in Faraday space is [equation (61) from Brentjens & de Bruyn 2005]

$$\psi \approx \frac{2\sqrt{3}}{\Delta(\lambda^2)}, \quad (18)$$

which is set by the observed wavelength-squared range $\Delta(\lambda^2) = \lambda_{max}^2 - \lambda_{min}^2$. Brentjens & de Bruyn (2005) note that equations (17) and (18) assume a top hat weight function that is unity between λ_{min} and λ_{max} and zero elsewhere. In general this will not be the case [cf. equations (20) and (21) presented shortly], requiring both ϕ_{max} and ψ to be determined empirically. For example, ψ may be fit with a Gaussian; this is analogous to fitting a Gaussian to an experiment-specific point spread function in aperture synthesis imaging. Combining equations (17) and (18), we find that $|\mathcal{F}^{cln}(\phi)|$ is effectively comprised of

$$M \equiv \frac{2\phi_{max}}{\psi} \quad (19)$$

independent samples, as was recognised by both George et al. (2011) and Macquart et al. (2012). In other words, no more than M statistically independent measurements of linearly polarized intensity may be extracted from $|\mathcal{F}^{cln}(\phi)|$, assuming \mathcal{F} is sampled with at least one trial ϕ per resolution element ψ . However, this description of M independent samples is only formally correct for ideally deconvolved signals. It is not appropriate for describing noise, which will consist of M independent samples that have been permanently correlated with one

another, due to the filtering nature of the discrete Fourier transform underlying the RM-synthesis technique. The presence of such correlations must be addressed to ensure a complete statistical description of L_{RM} . Further below, we describe how the noise term σ_{RM} may be defined so as to account for such correlations, enabling the notion of M independent samples to be effectively maintained. We note that the statistics describing measurements of $|\mathcal{F}^{cln}(\phi_t)|$ for some fixed trial Faraday depth ϕ_t (using the subscript t momentarily for clarity), are given by those of L from § 2. This is because for each trial ϕ_t , RM-synthesis essentially unwraps the observed spectral Q and U data in the complex plane so that their band-averaged values may be used to compute $\mathcal{F}(\phi_t)$. Denoting the number of observed spectral channels by T , we note that the form of equation (17) ensures that $M > T$ for $T > 1$; only for the trivial case $T = 1$ does $M = T$.

In this work we assume that \mathcal{F} consists of unresolved (Faraday-thin) components. We also assume that \mathcal{F}^{cln} has been cleaned (e.g. with RM-CLEAN; Heald et al. 2009) in an idealised manner (which may not be met in practise for RM spread functions exhibiting strong sidelobes) to prevent components in the spectrum from being contaminated by sidelobes from other components. Therefore, L_{RM} as defined in equation (2) can be characterised as the maximum of M independent samples within a cleaned Faraday dispersion spectrum, each of which exhibits the statistics of L discussed in § 2, and each of which may or may not contain any true underlying signal L_0 . For completeness, we note that the sequential processing techniques of RM-synthesis and deconvolution require signal sparsity in ϕ -space (cf. aperture synthesis imaging and the image sparsity requirement of the CLEAN technique; Cornwell, Braun, & Briggs 1999). For this work, we therefore require that the majority of M independent samples in \mathcal{F} are signal-free (i.e. with $L_0 = 0$). We do not consider the analysis of non-sparse Faraday dispersion spectra.

We denote the noise term for L_{RM} by σ_{RM} . We define this term as [note equation (38) from Brentjens & de Bruyn 2005]

$$\sigma_{RM} = \left[\frac{1}{\eta} \frac{\sum_{i=1}^T w_i^2 \sigma_{Q,U,i}^2}{\left(\sum_{i=1}^T w_i\right)^2} \right]^{\frac{1}{2}}, \quad (20)$$

where $\sigma_{Q,U,i}$ is the noise in the i 'th channel, η is a correction factor described shortly, and w_i are weighting factors for the observational data in each i 'th channel. For example, the channel weights may be chosen using least squares,

$$w_i = \frac{1}{\sigma_{Q,U,i}^2}, \quad (21)$$

noting as in § 2 that the analysis in this section is only formally valid for $\sigma_{Q,U,i} = \sigma_{Q,i} = \sigma_{U,i}$ in each i 'th channel; see Appendix A for discussion regarding $\sigma_{Q,i} \neq \sigma_{U,i}$. The factor η in equation (20) is required to account for correlations between samples of $|\mathcal{F}^{cln}(\phi)|$ at different depths ϕ . For clarity, we note that if L_{RM} were defined by $|\mathcal{F}^{cln}(\phi_t)|$ for fixed ϕ_t , then $\eta = 1$ would be appropriate because issues regarding selection of the maximum of > 1 correlated samples would be inapplicable. Moving on, we assume an experimental setup where the total number of trial ϕ samples across \mathcal{F} is given by

$$\kappa = \frac{2\phi_{max}}{\delta(\phi)} + 1, \quad (22)$$

where each sample is spaced apart by $\delta(\phi)$; i.e. a sampling rate of κ/M per ψ . The autocorrelation function is given by the magnitude of the RMSF for positive Faraday depths, which we denote by $|R_h| \equiv |R[h\delta(\phi) \geq 0]|$ with integer index $h = 0, \dots, \kappa - 1$, assuming an RMSF with span $\pm 2\phi_{max}$. Given positive correlation between samples, as will always be the case given $|R_h|$, estimates of σ_{RM} obtained using equation (20) with $\eta = 1$ will always underestimate the true value. A correction for this bias is given by Anderson [1971; see equation (51) in chapter 8, adjusted to represent sample variance] as

$$\eta = 1 - \frac{2}{\kappa - 1} \sum_{h=1}^{\kappa-1} \left(1 - \frac{h}{\kappa}\right) |R_h|. \quad (23)$$

Using the details above, we now derive the PDF for L_{RM} in the context of order statistics (e.g. David & Nagaraja 2003), first assuming $L_0 = 0$ in all M samples, then extending to the scenario where 1 of M samples in the Faraday dispersion spectrum contains an underlying signal $L_0 > 0$ (i.e. a single Faraday-thin component). We will not extend this derivation to the more general scenario in which each independent sample in the Faraday dispersion spectrum may have its own independent value of $L_0 \geq 0$ (i.e. multiple Faraday-thin components), though in principle the relevant PDF for this situation could be derived using elements from the derivations below. However, we do discuss detection thresholds for this scenario in § 4.3. Additionally, we will not attempt to derive PDFs for fully general scenarios in which resolved polarized emission in Faraday space (i.e. Faraday-thick components) may be present⁶.

For a sample of N independent and identically-distributed variates X_1, X_2, \dots, X_N ordered such that $X_{(1)} < X_{(2)} < \dots < X_{(N)}$ (using notation $X_{(j)}$ for ordered variates and X_j for unordered variates), then $X_{(k)}$ is known as the k 'th order statistic and $X_{(N)} = \max(X_j)$. If X has PDF $f(X)$ and CDF $F(X)$, then David & Nagaraja (2003) give the PDF for $X_{(k)}$ as

$$f(X_{(k)}) = \frac{N!}{(k-1)!(N-k)!} \frac{\{F[X_{(k)}]\}^{k-1}}{\{1-F[X_{(k)}]\}^{k-N}} f[X_{(k)}]. \quad (24)$$

Assuming absence of an underlying input signal ($L_0 = 0$), the PDF for L_{RM} is derived by substituting equations (11) and (14) into equation (24) with $N = M$ and $k = M$, giving

$$f(L_{RM}|M, L_0 = 0) = M \frac{L_{RM}}{\sigma_{RM}^2} \exp\left(-\frac{L_{RM}^2}{2\sigma_{RM}^2}\right) \times \left[1 - \exp\left(-\frac{L_{RM}^2}{2\sigma_{RM}^2}\right)\right]^{M-1}, \quad (25)$$

where $L_{RM} \geq 0$. Equation (25) is displayed for several values of M in the middle panel of Fig. 1; as M increases, for example as a result of increasing the spectral resolution in an experiment, so do the resulting measured intensities.

⁶ A systematic positive bias in Faraday space, similar to that referred to in the image plane as peak bias by Hales et al. (2012), will need to be accounted for when measuring the peak polarized intensity for resolved (Faraday-thick) sources.

The expectation value⁷ for equation (25) is obtained using integration by parts, a Taylor expansion, and term-wise integration, giving

$$\begin{aligned} E(L_{RM}|M, L_0 = 0) &= \int_0^\infty L_{RM} f(L_{RM}|L_0 = 0) dL_{RM} \\ &= \sqrt{\frac{\pi\sigma_{Q,U}^2}{2}} \sum_{S=1}^M \left[S^{-\frac{1}{2}} (-1)^{S-1} \times \frac{M!}{(M-S)! S!} \right]. \end{aligned} \quad (26)$$

Equation (26) limits to equation (12) when $M = 1$. Equation (26) represents the mean value of L_{RM} that will be observed for a line of sight containing no polarized emission ($L_0 = 0$). Asymptotically, this mean value grows as $\approx \sqrt{\ln M}$ (David & Nagaraja 2003).

We now extend our derivation to the scenario where $M-1$ independent signal-free samples are drawn from equation (11) and 1 sample with arbitrary $L_0 > 0$ is drawn from equation (6), such that L_{RM} represents the observed maximum of these M samples. The distribution for the maximum intensity value of $M-1$ signal-free samples, which we denote L_{M-1} , is derived in the same manner as equation (25), but with $N = k = M-1$. Following David & Nagaraja (2003), the CDF for $L_{RM} = \max(L_{M-1}, L)$ is then given by

$$F(L_{RM}|M, L_0) = F(L_{M-1}|M, L_0 = 0) F(L|L_0). \quad (27)$$

The PDF for L_{RM} is therefore

$$\begin{aligned} f(L_{RM}|M, L_0) &= \frac{d}{dL_{RM}} F(L_{RM}|M, L_0) \\ &= f(L_{M-1}|M, L_0 = 0) F(L|L_0) + \\ &\quad F(L_{M-1}|M, L_0 = 0) f(L|L_0) \\ &= \frac{L_{RM}}{\sigma_{RM}^2} \exp\left(-\frac{L_{RM}^2}{2\sigma_{RM}^2}\right) \times \\ &\quad \left[1 - \exp\left(-\frac{L_{RM}^2}{2\sigma_{RM}^2}\right)\right]^{M-1} \times \\ &\quad \left\{ (M-1) \left[1 - \exp\left(-\frac{L_{RM}^2}{2\sigma_{RM}^2}\right)\right]^{-1} \times \right. \\ &\quad \left. \left[1 - \mathcal{Q}_1\left(\frac{L_0}{\sigma_{RM}}, \frac{L_{RM}}{\sigma_{RM}}\right)\right] + \right. \\ &\quad \left. \exp\left(-\frac{L_0^2}{2\sigma_{RM}^2}\right) I_0\left(\frac{L_{RM}L_0}{\sigma_{RM}^2}\right) \right\}, \end{aligned} \quad (28)$$

where $L_{RM} \geq 0$. Equation (28) is displayed for several values of L_0/σ_{RM} for an $M = 30$ observing setup in the bottom panel of Fig. 1; $M = 30$ has been selected for illustrative simplicity, as suitable for a 1.4 GHz observation with 200 MHz bandwidth split into 24 spectral channels. The expectation value for equation (28),

$$E(L_{RM}|L_0) = \int_0^\infty L_{RM} f(L_{RM}|L_0) dL_{RM}, \quad (29)$$

⁷ We note that a derivation of the expectation value for the signal-free case is attempted by Heald et al. (2009), where they equate the $(M-1)/M$ quantile of the CDF with the expected value of the largest order statistic. A better approximation is $M/(M+1)$; see equation (4.5.1) from David & Nagaraja (2003). We present the exact solution in equation (26).

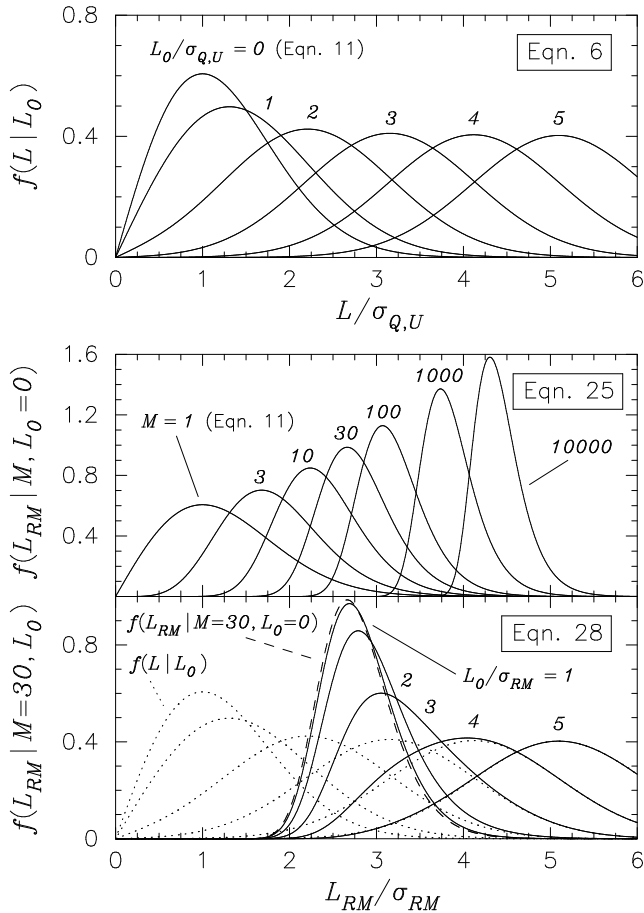


Figure 1. *Top:* The Ricean distribution, equation (6), displayed for several values of true polarization SNR $L_0/\sigma_{Q,U}$. When $L_0 = 0$ the Ricean distribution limits to the Rayleigh distribution, equation (11). *Middle:* The distribution for L_{RM} with $L_0 = 0$, equation (25), displayed for several values of M , the effective number of independent samples in $|\mathcal{F}^{cln}(\phi)|$ as defined by equation (19). This panel illustrates how different values of M affect the mean value of L_{RM} for lines of sight free from polarized emission ($L_0 = 0$). When $M = 1$, equation (25) limits to the Rayleigh distribution, equation (11). *Bottom:* The distribution for L_{RM} , equation (28), displayed for the $M = 30$ case (as suitable for a 1.4 GHz observation with 200 MHz bandwidth split into 24 spectral channels) for several SNRs L_0/σ_{RM} . As L_0/σ_{RM} increases, equation (28) limits to the Ricean distribution (dotted curves, replicated from top panel). However, unlike a Ricean distribution, as $L_0/\sigma_{RM} \rightarrow 0$, equation (28) limits to the signal-free distribution from equation (25) (dashed curve, replicated from middle panel).

does not appear to have an analytic solution; it may be evaluated numerically. As with the Ricean distribution, the distribution for L_{RM} is signal-dependent, positively skewed, and leptokurtic. When the magnitude of L_0 is comparable to the noise σ_{RM} , the distribution for L_{RM} will approach the signal-free case from equation (25). For larger L_0/σ_{RM} , the distribution will approach the Ricean distribution from equation (6).

The results presented in this section provide a theoretical explanation for the empirical curves presented in Fig. 4 of George et al. (2011) for their specific experimental setup. Parameterised by M , the equations above enable statisti-

cal characteristics of L_{RM} to be quantified for a range of experimental setups.

Furthermore, our results provide an explanation for the discrepancy between the simulated and theoretical PDFs presented in the lower panel of Fig. 6 from Macquart et al. (2012), in which the effects of correlation were not considered. To demonstrate, we evaluated equation (23) for an RMSF representing an experimental setup similar to that described by Macquart et al. (2012), with 24×8 MHz channels between 1296 and 1480 MHz, and Faraday space sampling given by $\delta(\phi) = 5 \text{ rad m}^{-2}$ with $\phi_{max} = 4000 \text{ rad m}^{-2}$. The result was $\sqrt{\eta} = 0.935$. Thus Macquart et al. (2012) overestimated their SNRs by $\sim 7\%$, consistent with their observed discrepancy⁸. (Note that the diminished peak density in their simulated PDF is accounted for by the Jacobian; their green curve is not normalised.)

3.1 Detection Significance

Following § 2.1, we quantify the Gaussian equivalent significance, denoted by G_{RM}^{ES} , for a measurement of L_{RM} by equating the CDF for L_{RM} (i.e. $F(L_{RM}|M, L_0 = 0)$, obtained by integrating equation (25)) with the standard confidence interval for a Gaussian, giving

$$|G_{RM}^{ES}|/\sigma_{RM} \equiv \sqrt{2} \text{erf}^{-1} \left(\left\{ 1 - \exp \left[-\frac{1}{2} \left(\frac{L_{RM}}{\sigma_{RM}} \right)^2 \right] \right\}^M \right). \quad (30)$$

Alternatively, equation (30) may be rearranged to quantify the linear polarization equivalent significance, denoted by L_{RM}^{ES} , for a measurement of G , giving

$$L_{RM}^{ES}/\sigma_{RM} \equiv \sqrt{-2 \ln \left\{ 1 - \left[\text{erf} \left(\frac{1}{\sqrt{2}} \frac{|G|}{\sigma_{RM}} \right) \right]^{1/M} \right\}}. \quad (31)$$

Examples illustrating use of these equations are presented in § 4. Equation (31), and thus implicitly equation (30), is displayed for several values of M in Fig. 2.

4 EXAMPLES

In § 4.1 and § 4.2 we construct examples to demonstrate use of the signal-free expectation value equations and significance relationships derived for L in § 2.1 and L_{RM} in 3.1, respectively. In § 4.3 we describe how the significance relationships for L_{RM} may be used to assess Faraday dispersion spectra comprising multiple unresolved Faraday components.

4.1 Standard Linear Polarization

The expectation value for a measurement of L for an emission-free ($L_0 = 0$) line of sight is given by equation (12); equivalently, equation (12) returns the average observed intensity for a spatial pixel situated away from real sources in

⁸ Separately, we note that Macquart et al. (2012) defined noise per channel (i.e. $\sigma_{Q,U,i}$) as the quadrature sum of $\sigma_{Q,i}$ and $\sigma_{U,i}$, so that $\sigma_{Q,U,i} = \sqrt{2}\sigma_{Q,i}$ for the case $\sigma_{Q,i} = \sigma_{U,i}$. As mentioned above and in § 2, a more appropriate definition is $\sigma_{Q,U,i} = \sigma_{Q,i} = \sigma_{U,i}$.

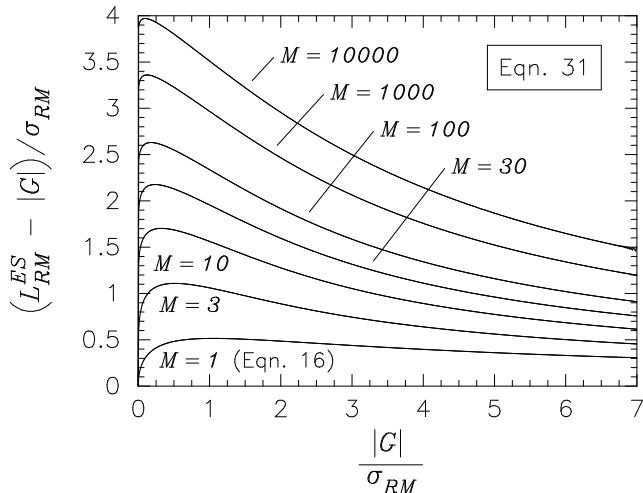


Figure 2. Detection thresholds for L_{RM} that exhibit equivalent Type I (false positive) error rates to those of standard Gaussian detections, G . The curves trace equation (31) for several values of M , limiting to equation (16) for $M = 1$.

an image of standard linear polarization, namely $\sim 1.25\sigma_{Q,U}$ (e.g. see behaviour of dashed curves in Fig. 3).

Using equation (15), we find that the detection of a linearly polarized source with $\text{SNR } L_{Q,U}/\sigma_{Q,U} = 4.0$ is equivalent in significance to the detection of a $\pm 3.6\sigma_{Q,U}$ source under Gaussian statistics.

Using equation (16) or the $M = 1$ curve from Fig. 2, we find that a detection threshold of $L/\sigma_{Q,U} = 5.4$ must be imposed in order to ensure that polarization detections have an equivalent Gaussian significance in excess of $\pm 5.0\sigma_{Q,U}$ (i.e. greater than 99.99994% confidence).

4.2 Faraday-Space Linear Polarization

The expectation value for a measurement of L_{RM} for an emission-free line of sight is given by equation (26); its value depends on M . Equivalently, equation (26) returns the average observed intensity for a spatial pixel situated away from real sources in an image of peak Faraday-space linear polarization, which for an example image with $M = 30$ is found to be $\sim 2.78\sigma_{RM}$ (e.g. see behaviour of solid curves in Fig. 3).

We now demonstrate the statistical significance relationships for L_{RM} with $M = 30$ using the same examples from § 4.1.

Using equation (30), we find the detection of a source with $L_{RM}/\sigma_{RM} = 4.0$ to be equivalent in significance to the detection of a $\pm 2.6\sigma_{Q,U}$ source under Gaussian statistics.

Using equation (31), we find that a detection threshold of $L_{RM}/\sigma_{RM} = 6.0$ is required to ensure equivalent Gaussian significance in excess of $\pm 5.0\sigma_{RM}$.

4.3 Multiple Unresolved Faraday Components

In § 3 we derived the PDF for L_{RM} by assuming that $|\mathcal{F}^{cln}(\phi)|$ contains no more than a single unresolved Faraday component. While derivations of PDFs for polarized intensity measurements drawn from more complicated Faraday dispersion spectra remain beyond the scope of this work,

we note that the single Faraday component assumption was not formally required to derive the significance relationships presented in § 3.1. Indeed, these relationships are suitable for assessing the Gaussian equivalent significance for any number of the available M statistically independent measurements in $|\mathcal{F}^{cln}(\phi)|$. This is because the relationships in effect benchmark the significance of any observed sample against the maximum theoretical noise sample expected within $|\mathcal{F}^{cln}(\phi)|$. Therefore, equations (30) and (31), as demonstrated in § 4.2, may be used to evaluate the Gaussian equivalent significance for each candidate Faraday component in $|\mathcal{F}^{cln}(\phi)|$; this practice will help to identify noise-induced components in complex Faraday dispersion spectra (e.g. see data obtained by Law et al. 2011).

5 SOURCE PROFILES IN POLARIZATION IMAGES

Two-dimensional images of linearly polarized intensity for L or L_{RM} may be formed by calculating equation (1) or (2), respectively, for each independent spatial pixel. In this section we illustrate cross-sectional profiles for astronomical sources as observed in images of linear polarization, to both demonstrate use of the equations derived earlier, and to briefly outline challenges that need to be met for robust image-plane source extraction. For demonstration we focus on the observation of sources with Gaussian morphologies; such sources are typically encountered in radio astronomy because of the well-approximated Gaussian nature of telescope point spread functions.

In Fig. 3 we trace mean observed spatial profiles through Gaussian sources, each with full width at half-maximum (FWHM) standardised to unity, that have been embedded in images for which the intensities of individual spatial pixels exhibit the statistics of either Gaussian noise, the distribution for L from equation (6), or the distribution for L_{RM} from equation (28) with $M = 30$; we assume infinitesimal pixel dimensions so as to ignore pixel discretisation effects. The curves displayed in Fig. 3 were obtained analytically using the following approach. First, we constructed true underlying SNR profiles for our Gaussian sources as spatial functions of fractional FWHM, x , using

$$\text{SNR}^{\text{true}}(x) = \text{SNR}_{\text{peak}}^{\text{true}} \exp \left[-4 \ln(2) \frac{x^2}{\text{FWHM}^2} \right]. \quad (32)$$

This equation can be used to represent underlying cross-sectional profiles for Gaussian sources in linear polarization, i.e. $L_0(x)$, noting that Gaussian profiles in images of Stokes Q and U remain Gaussian through equation (5). To obtain observed spatial profiles for the Gaussian noise (denoted by G), L , and L_{RM} images, we then computed expectation values as a function of x for the input signal defined by equation (32). For the Gaussian noise profiles, expectation values for observed SNRs equal their true underlying SNRs (i.e. expectation values in Gaussian noise are signal-independent; i.e. $\langle \text{SNR}^{\text{obs}}(x) \rangle = \text{SNR}^{\text{true}}(x)$, $\forall x$). The expectation values for $L(x)$ and $L_{RM}(x)$ were computed using equations (9) and (29), respectively, with $L_0(x)$ given by equation (32). In signal-free regions (i.e. left and right of the sources), $\langle L(x) \rangle$ and $\langle L_{RM}(x) \rangle$ limit to equations (12) and (26), respectively.

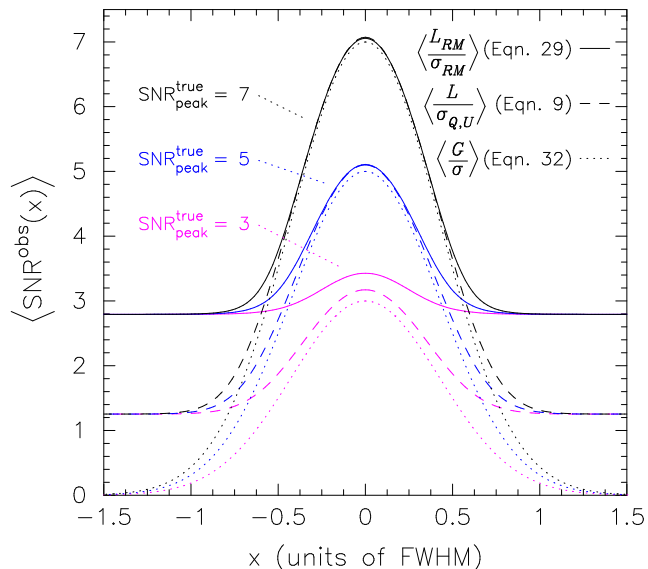


Figure 3. Mean spatial profiles observed for Gaussian sources embedded within images exhibiting Gaussian (dotted curves), L (dashed curves), and L_{RM} (for $M = 30$; solid curves) pixel intensity statistics, displayed for several input true peak SNRs. See § 5 for details.

As $\text{SNR}_{\text{peak}}^{\text{true}}$ increases, the curves for $\langle L(x) \rangle$ and $\langle L_{RM}(x) \rangle$ limit to the Gaussian case, the latter more slowly (cf. Fig. 1).

Least squares 2D elliptical Gaussian fitting routines (e.g. the task `IMFIT` from the `MIRIAD` package; Sault et al. 1995) are typically used to extract sources from images exhibiting Gaussian noise. The polarization profiles in Fig. 3 suggest that Gaussian fitting routines may not be appropriate for source extraction in images of linear polarization, unless low SNR wings are excluded from the fitting process (e.g. by imposing a SNR cut-off threshold for fitting). Additionally, the non-Gaussian distribution of pixel intensities about the mean profiles illustrated in Fig. 3 will likely cause a systematic positive bias in extracted flux densities, particularly for low SNR sources. To address these challenges, detailed inspections regarding the accuracy of source extraction methods in images of linear polarization are required. Such analysis is beyond the scope of this work; see Hales et al. (2012) for an analysis of source extraction in linear polarization.

6 NON-GAUSSIAN NOISE IN Q/U ?

George et al. (2011) recently suggested that aperture-synthesis imaging and calibration artefacts may introduce strong non-Gaussianities into the noise distribution for images of Stokes Q and U , which will in turn affect the false detection rate of sources in linear polarization. To model these non-Gaussianities in Stokes Q and U , they suggested use of a compound distribution comprising a Gaussian distribution plus an exponential distribution; this is known from the psychological literature as the Ex-Gaussian distribution (Hohle 1965; Burbeck & Luce 1982).

While it is likely that imaging artefacts will be present in images of Stokes Q and U , their influence should be largely accounted for in *local* estimates of rms noise (see e.g.

Hales et al. 2012). This process will ensure that the distribution of pixel SNRs is well described by a Gaussian, in turn ensuring that local detection thresholds can be computed accurately using the equations presented in this paper.

In an effort to explain the seemingly non-Gaussian distribution exhibited in the lower panel of Fig. 7 from George et al. (2011), in which Stokes Q data from the NVSS (Condon et al. 1998) were presented, we focus on two effects. We note that George et al. (2011) did not evaluate false detection rates using the NVSS data itself, but rather a simulated sky survey described as having characteristics similar to the NVSS. Here we examine whether the real NVSS data can be used to justify claims of strong non-Gaussian noise.

The first consideration is the presence of real sources, which may be positive or negative in Stokes Q (or U). Such sources need to be masked prior to investigation of the noise distribution. George et al. (2011) masked real total intensity sources out of the Stokes Q NVSS data investigated. We attempted to recover a non-Gaussian distribution using NVSS data by investigating a sample of $4^\circ \times 4^\circ$ tiles selected to have central positions located along a line of constant declination with J2000 $\delta = +28^\circ$; for simplicity we did not analyse the full 2326 tiles comprising the NVSS. We selected 75 of the 90 tiles in this declination range, avoiding 15 tiles containing missing pointings in Stokes Q . We supplemented this sample with an additional tile, C1232P12, chosen arbitrarily to ensure that at least one tile containing pointings with significant amplitude calibration errors was included in our analysis. Thus our raw data sample consisted of 76 tiles. We also investigated a subset of 73 of these tiles following the removal of tile C1232P12, as well as two other tiles, C0432P28 and C0448P28, which were found to contain pointings with minor yet distinct calibration errors. The declination range above was selected to be representative of the NVSS, comprising tiles positioned from the North Galactic Pole down to and below the Galactic plane. Tiles near the Galactic plane are likely contain large-scale emission unresolved by the NVSS, which may in turn plausibly introduce non-Gaussianities into the data due to difficulties encountered during deconvolution (e.g. Cornwell, Braun, & Briggs 1999). To obtain Stokes Q images as free from true sources as possible, we conservatively masked all pixels that had corresponding Stokes I intensities > 0 mJy beam $^{-1}$. The rms noise in the NVSS is $\sigma_I \approx 0.45$ mJy beam $^{-1}$ in Stokes I and $\sigma_Q \approx 0.29$ mJy beam $^{-1}$ in Stokes Q . Therefore, we note that if masking were only applied to pixels corresponding to catalogued NVSS sources, namely pixels with $I \gtrsim 4.5\sigma_I$, then real Stokes Q emission from sources with $\sim 20\%$ fractional polarization could remain unmasked with significance up to $Q \approx 1.4\sigma_Q$, biasing efforts to uncover the underlying noise distribution. We then compared histograms of Stokes Q pixels intensities for the unmasked and masked data, and for the distribution observed by George et al. (2011), as shown in the upper panel of Fig. 4. We found that the unmasked 76 tile data displayed non-Gaussian wings above the NVSS levels reported by George et al. (2011), while the masked 76 tile data displayed wings that fell off more rapidly with intensity than their levels. The 73 tile data was found to exhibit significantly attenuated wings compared with the 76 tile data. The distribution described by George et al. (2011) is inconsistent with the 73 tile data. The difference between the unmasked and masked 76 tile data in Fig. 4 is due to

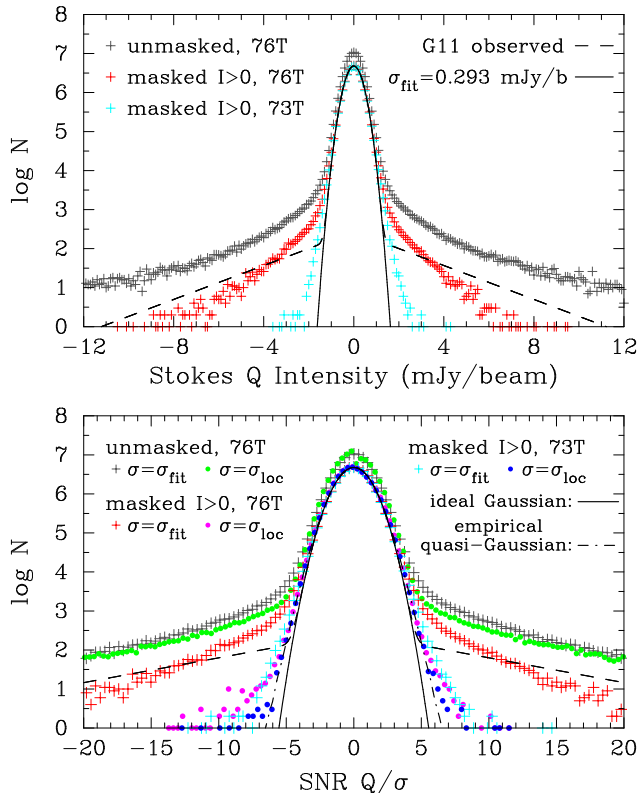


Figure 4. *Upper panel:* Distribution of Stokes Q pixel intensities using all pixels (gray points) or only those with corresponding Stokes I pixel intensities ≤ 0 mJy beam $^{-1}$ (red points) for our full sample of 76 NVSS tiles (76T). The cyan points represent the masked distribution for our 73 tile sample (73T), following removal of 3 tiles containing pointings with easily discerned imaging errors. The solid curve is a fitted Gaussian to the 73T points, with $\sigma_{\text{fit}} = 0.293$ mJy beam $^{-1}$. The dashed curve is from the lower panel of Fig. 7 from George et al. (2011) for their observed NVSS data. *Lower panel:* Distribution of pixel SNRs corresponding to the points in the upper panel, obtained by assuming constant $\sigma = \sigma_{\text{fit}}$ or using local rms noise estimates $\sigma = \sigma_{\text{loc}}$. The solid curve is a Gaussian with unit variance. The dot-dashed curve, obtained empirically, predicts the distribution of pixel SNRs that will be observed when rms noise values exhibit 10% error. The dashed curve represents the corresponding upper panel curve, normalised by σ_{fit} . Note that x-axes are not matched between upper and lower panels.

real sources, while the difference between the masked 76 and 73 tile data is due to the inclusion of tiles with significant imaging errors. Therefore, the discrepancy between the NVSS distribution observed by George et al. (2011) and the masked 73 tile NVSS distribution examined in this work is likely to be due to residual unmasked sources, the inclusion of corrupted tiles, a combination of both, or some other processing error.

To explain why the masked 73 tile data exhibit small non-Gaussian wings, we now consider a second effect that may also lead to spurious claims of non-Gaussian noise. It is common for rms noise to vary spatially throughout an image due to imaging artefacts about strong sources, or intrinsic observational features such as primary beam sensitivity. If a histogram of pixel intensities is used as a proxy to examine the noise distribution within such an image, rather than a

histogram of pixel SNRs (which require local rms noise estimates), then the inferred noise distribution will appear to follow a Gaussian distribution with exponential wings. Similarly, if the distribution of pixel SNRs is examined for these images whilst assuming that rms noise is spatially uniform, then the inferred noise distribution will again appear to follow the Ex-Gaussian distribution. In both these examples, no intrinsic non-Gaussianities need exist. To demonstrate, consider the following illustrative scenario in which an image is arbitrarily divided into two spatial regions, each represented by Gaussian statistics but with a different standard deviation. If 99.9% of the image has standard deviation 1 (in arbitrary units) and 0.1% has standard deviation 5 (this is a crude representation of the fraction of 76 Stokes Q tiles exhibiting calibration errors), then the observed distribution of all pixel intensities will follow an Ex-Gaussian distribution. Despite this suggested appearance of non-Gaussianity, the distribution of pixel SNRs, obtained using local rms noise estimates, will exhibit purely Gaussian characteristics. Indeed, this simplified example further demonstrates that if an observed distribution of pixel SNRs is not Gaussian (following masking of real sources), then the implemented local rms noise estimation procedure may not be performing suitably.

To construct distributions of pixel SNRs for the unmasked and masked NVSS data presented above, we used the rms estimation algorithm implemented within the **SExtractor** package (Bertin & Arnouts 1996; Holwerda 2005) to generate a background rms noise map for each tile. We set the local mesh size to 24×24 pixel 2 , an area equivalent to $N_b = 50$ independent resolution elements (see Hales et al. 2012). Our estimates of local rms noise therefore have uncertainty $\{[1 + 0.75/(N_b - 1)]^2 [1 - N_b^{-1}] - 1\}^{0.5} \approx 10\%$ (using an approximation to the uncertainty of the standard error estimator, suitable for $N_b > 10$; see p. 63 of Johnson & Kotz 1970), or greater if many resolution elements in a given mesh contain true sources. We then computed pixel SNRs using the local rms noise values. For comparison, we also computed pixel SNRs by assuming a spatially uniform rms noise value for all tiles. This value was obtained from a fit to the masked 73 tile pixel intensity data, as indicated by the solid curve in the upper panel of Fig. 4. The resulting SNR histograms for the unmasked and masked NVSS data are presented in the lower panel of Fig. 4. We found that the distributions constructed using the uniform noise level exhibited stronger non-Gaussian wings than those constructed using local noise estimates (the former are equivalent to the pixel intensity distributions presented in the upper panel of Fig. 4), indicating the presence of spatial variations in image sensitivity. This is most clearly demonstrated by the masked 76 tile data; the failure of this data to exhibit a pure Gaussian distribution when using local noise estimates may be predominantly attributed to rapid changes in image sensitivity near corrupted pointings, where the accuracy of the rms noise estimation algorithm employed by **SExtractor** is diminished. The SNR distribution for the masked 73 tile data with local rms noise estimates (blue dots) was found to closely follow a Gaussian distribution, modulo two apparently non-Gaussian features. First, neglecting bins with $|\text{SNR}| \gtrsim 6$, the distribution was found to broaden with SNR against that of a true Gaussian. This broadening is predominantly due to variance in the rms noise estimates used to calculate SNRs, rather than any in-

trinsic features of the pixel intensity data. To demonstrate, we simulated a distribution of SNRs by drawing samples from a Gaussian with unit variance and dividing each sample by a noise term that was itself drawn from a Gaussian with unit mean and standard deviation 10%. The resulting distribution is displayed in the lower panel of Fig. 4, providing a close fit to the observed data. Second, the distribution was found to exhibit 18 pixels with $|\text{SNR}| > 7$. We examined the NVSS image data to determine the origin of these discrepant pixels. We found that 5 of these pixels were situated one pixel beyond the masking boundary of a strong total intensity source, where the total intensity emission was observed to drop suddenly to become negative due to an adjacent noise trough or possibly a cleaning artefact. These Stokes Q pixels were thus associated with unmasked real emission. The remaining 13 pixels were situated within pointings exhibiting image striping, consistent with calibration errors; additionally, each of these pointings were situated close to the Galactic plane, with Galactic longitude $\sim 80^\circ$ and latitude $\sim -15^\circ$. Given these identifications, we conclude that there is no significant evidence for non-Gaussian noise in the Stokes Q NVSS data once pointings exhibiting easily discerned calibration errors have been removed. While we cannot rule out the presence of non-Gaussian noise in all surveys, the lack of evidence for such noise in the NVSS sample analysed here suggests that surveys with more sophisticated data reduction are unlikely to be affected, and almost certainly not at the strong levels suggested by George et al. (2011).

7 CONCLUSIONS AND FUTURE WORK

We have derived customised statistics to describe Faraday-space measurements of linearly polarized intensity obtained using RM synthesis. The equations presented enable objective determination of the significance of polarization detections, which will be useful for upcoming surveys of radio polarization.

We found that when the observation-specific parameter M was increased, larger detection thresholds were required for L_{RM} to ensure that noise features were not mistaken for real polarized emission (e.g. see middle panel of Fig. 1). We found this effect to be exponential; M needed to be increased by at least an order of magnitude (e.g. from 10 to 100, or 1,000 to 10,000) before the new detection threshold required to satisfy an original level of statistical significance needed to be significantly raised. Therefore, we conclude that it is of limited practical use to tailor observational setups to minimise M , unless M can be reduced by at least an order of magnitude. A suitable strategy for large- M observations, such as those afforded by the $M > 10^4$ capabilities of facilities such as the Australia Telescope Compact Array and Expanded Very Large Array, may be to first perform RM-synthesis using reduced spectral resolution (i.e. by averaging spectral channels to reduce T , and in turn M) in order to identify faint polarized emission over a reduced $\pm\phi_{max}$ range.

We also discussed source extraction in polarization images and the importance of obtaining spatially-dependent rms noise estimates.

We have not discussed the derivation of confidence intervals for polarization measurements, the setting of up-

per limits, or polarization bias. While detailed inspection of these issues remains beyond the scope of this work, we close by briefly highlighting how our results may be used in the future to address each of them, as follows.

Using the equations developed in this work, credible intervals (the Bayesian equivalent of frequentist confidence intervals) may be constructed using the technique presented by Vaillancourt (2006). Similarly, confidence bounds (which depend on observed intensities) and upper limits (which do not depend on observed intensities, but rather on the detection process and Type II error minimisation) may be evaluated using the techniques presented by Kashyap et al. (2010); a demonstration using observational data will be presented by Hales et al. (in preparation).

Finally, we note that the different statistics exhibited by L and L_{RM} prevent the application of polarization debiasing schemes designed for the former (e.g. Simmons & Stewart 1985; Leahy & Fernini 1989) from being applied to the latter. However, exceptions may be suitable in the limit to polarized sources strong enough to display a similar PDF in both L_{RM} and L (e.g. compare curves in the lower and upper panels of Fig 1). In general, a polarization bias correction scheme designed for L_{RM} would need to be parameterised by a term such as M from equation (19), so as to take into account the experiment-specific terms ϕ_{max} and ψ . We note that the fixed, un-parameterised debiasing schemes presented by George et al. (2011) and Macquart et al. (2012) are therefore limited in applicable experimental scope. Future investigations are clearly required to resolve these issues. Instead of attempting to correct observed flux densities for polarization bias alone, an alternate approach may be to combine this correction with one for Eddington (1913) bias, which like polarization bias is always present. A demonstration of this combined technique to remove both polarization and Eddington bias will be presented by Hales et al. (in preparation).

ACKNOWLEDGMENTS

We thank Tim Cornwell and Samuel Müller for helpful discussions. We thank the anonymous referee for comments that led to the improvement of this paper. C. A. H. acknowledges the support of an Australian Postgraduate Award and a CSIRO OCE Scholarship. B. M. G. acknowledges the support of an Australian Laureate Fellowship from the Australian Research Council through grant FL100100114.

REFERENCES

- Anderson T. W., 1971, *The Statistical Analysis of Time Series*. John Wiley & Sons, New York, NY
- Bertin E., Arnouts S., 1996, *A&AS*, 117, 393
- Brentjens M. A., de Bruyn A. G., 2005, *A&A*, 441, 1217
- Burbeck S. L., Luce R. D., 1982, *Perception and Psychophysics*, 32, 117
- Burn B. J., 1966, *MNRAS*, 133, 67
- Clifford A. A., 1973, *Multivariate Error Analysis*. Applied Science Publishers, London
- Condon J. J., Cotton W. D., Greisen E. W., Yin Q. F.,

- Perley R. A., Taylor G. B., Broderick J. J., 1998, *AJ*, 115, 1693
- Cornwell T., Braun R., Briggs D. S., 1999, *ASPC*, 180, 151
- David H. A., Nagaraja H. N., 2003, *Order Statistics* (3rd ed.). John Wiley & Sons, Hoboken, NJ
- Deboer D. R., et al., 2009, *IEEE Proceedings*, 97, 1507
- Eddington A. S., 1913, *MNRAS*, 73, 359
- Gaensler B. M., Landecker T. L., Taylor A. R., POSSUM Collaboration, 2010, *BAAS*, 42, 515
- George S. J., Stil J. M., Keller B. W., 2011, *PASA*, in press (arXiv:1106.5362)
- Hales C. A., Murphy T., Curran J. R., Middelberg E., Gaensler B. M., Norris R. P., 2012, *MNRAS*, in press
- Heald G., Braun R., Edmonds R., 2009, *A&A*, 503, 409
- Hohle R. H., 1965, *Journal of Experimental Psychology*, 69, 382
- Holwerda B. W., 2005, arXiv:astro-ph/0512139
- Huynh M. T., Jackson C. A., Norris R. P., Prandoni I., 2005, *AJ*, 130, 1373
- Johnson N. L., Kotz S., 1970, *Distributions in Statistics: Continuous Univariate Distributions—1*. Houghton Mifflin, NY
- Johnston S., et al., 2008, *Experimental Astronomy*, 22, 151
- Kashyap V. L., van Dyk D. A., Connors A., et al., 2010, *ApJ*, 719, 900
- Law C. J., Gaensler B. M., Bower G. C., et al., 2011, *ApJ*, 728, 57
- Leahy P., Fernini I., 1989, *VLA Scientific Memorandum No. 161*, NRAO
- Macquart J.-P., Ekers R. D., Feain I., Johnston-Hollitt M., 2012, *ApJ*, 750, 139
- Marcum J. I., 1948, *RAND Research Memo*, RM-753, (Reprinted in 1960, *IRE Transactions on Information Theory*, IT-6, 59)
- Perley R. A., Chandler C. J., Butler B. J., Wrobel J. M., 2011, *ApJL*, 739, L1
- Rayleigh J. W. S., 1880, *Philosophical Magazine*, 5th Series, 10, 73
- Rice S. O., 1945, *Bell System Technical Journal*, 24, 46; Reprinted by Wax N., 1954, *Selected Papers on Noise and Stochastic Processes*. Dover Publications, NY, p. 133
- Sault R. J., Teuben P. J., Wright M. C. H., 1995, *Astronomical Data Analysis Software and Systems IV*, 77, 433
- Simmons J. F. L., Stewart B. G., 1985, *A&A*, 142, 100
- Simon M. K., 1998, *IEEE Commun. Lett.*, 2, 39
- Taylor A. R., Salter C. J., 2010, in *Kothes R., Landecker T. L., Willis A. G., eds, ASP Conf. Ser. Vol. 438, The Dynamic Interstellar Medium: A Celebration of the Canadian Galactic Plane Survey*. Astron. Soc. Pac., San Francisco, p. 402
- Vaillancourt J. E., 2006, *PASP*, 118, 1340
- Wilson W. E., et al., 2011, *MNRAS*, 416, 832

APPENDIX A: UNEQUAL NOISE IN Q/U

Derivation of the PDF for L with $\sigma_Q \neq \sigma_U$ requires marginalising the Euclidean norm of a bivariate normal distribution over position angle, resulting in a complicated analytic expression that is difficult to utilise and is more easily obtained and analysed numerically. Given that $\sigma_Q \neq \sigma_U$ may be encountered in observational data, as highlighted in the

examples below, in this Appendix we investigate how $\sigma_{Q,U}$ may be defined such that the analytic equations presented in this work for L and L_{RM} may remain *approximately* valid. While it is not possible to fully model a bivariate normal distribution with a single noise term $\sigma_{Q,U}$ when $\sigma_Q \neq \sigma_U$, we note that the only region of PDF parameter space that needs to be accurately modelled is that of the noise outlier population (i.e. $\gtrsim 5\sigma$); in practice, detection thresholds may be suitably defined using this population, such that accurate modelling of the remaining parameter space is not required. We therefore focus here on obtaining a rudimentary definition for $\sigma_{Q,U}$ that, under certain conditions, may facilitate use of the analytic relationships presented in this work.

Two examples of data exhibiting $\sigma_Q \neq \sigma_U$ are as follows. First, consider images of Stokes Q and U in which a polarized source is present with signal $Q_0 \neq U_0$, as will be the case in general. Following deconvolution, it is possible for residual sidelobes and other artefacts about strong sources to affect one image more than the other, causing some lines-of-sight to exhibit $\sigma_Q \neq \sigma_U$. As a second example, spatial variations in root-mean-square (rms) noise may be present and independently-positioned throughout images of Stokes Q and U , where beam-sized noise elements are superposed on larger-scale undulations. For example, undulations in rms noise may be produced in aperture synthesis images by large scale emission that is unrecoverable by deconvolution algorithms such as CLEAN (Cornwell, Braun, & Briggs 1999), or in general radio imaging through insufficient flagging of data affected by radio frequency interference. Even surveys designed to exhibit spatially uniform rms noise, such as the NVSS (Condon et al. 1998), exhibit undulations in rms noise due to a combination of the effects described above, thus enabling some lines of sight to exhibit $\sigma_Q \neq \sigma_U$. Though the issues above may be mitigated by telescope design, observing strategy, and data processing, the potential remains for lines-of-sight to exhibit $\sigma_Q \neq \sigma_U$. Additionally, and in a trivial sense, uncertainties in the estimator used to evaluate $\hat{\sigma}_Q$ and $\hat{\sigma}_U$ (using hat notation here to indicate standard errors rather than true underlying standard deviations) will result in $\hat{\sigma}_Q \neq \sigma_Q$ and $\hat{\sigma}_U \neq \sigma_U$, such that $\hat{\sigma}_Q \neq \hat{\sigma}_U$ may result in situations where $\sigma_Q = \sigma_U$. For example, if a mesh containing $N_b < 100$ independent resolution elements is used to estimate the local standard error in an image (e.g. as demonstrated in Stokes I by Huynh et al. 2005), then the uncertainty in this estimator will be $> 7\%$ (using the formula referenced in-text in § 6). Given this and the examples above, how should $\sigma_{Q,U}$ be defined? Ideally, when $\sigma_Q \neq \sigma_U$, the use of $\sigma_{Q,U}$ should be avoided altogether and all analysis should be conducted numerically to correctly utilise the true PDF. However, this may be cumbersome for typical situations where $\hat{\sigma}_Q$ and $\hat{\sigma}_U$ are within a factor of, say, $\sim 10\%$.

We begin by focusing on L and noting that in situations where $\sigma_Q = \sigma_U$, a suitable definition for $\sigma_{Q,U}$ may be given by $0.5(\hat{\sigma}_Q + \hat{\sigma}_U)$; this solution is more precise (i.e. exhibits less dispersion about the true standard deviation) than assigning $\sigma_{Q,U} = \hat{\sigma}_Q$ (or $\sigma_{Q,U} = \hat{\sigma}_U$), because the probability of $\hat{\sigma}_Q$ overestimating the true standard deviation is greater than the probability of both $\hat{\sigma}_Q$ and $\hat{\sigma}_U$ overestimating it. Similar performance may be obtained by defining $\sigma_{Q,U}$ following first-order error propagation (e.g. Clifford 1973) evaluated about the point (Q_0, U_0) ,

$$\sigma_{Q,U}^2 \approx \left[\frac{\partial L}{\partial Q}(Q_0) \right]^2 \sigma_Q^2 + \left[\frac{\partial L}{\partial U}(U_0) \right]^2 \sigma_U^2. \quad (\text{A1})$$

We note that neglectation of higher-order terms in the equation above is formally incorrect (such terms are important when noise dominates signal); however, our rudimentary interest here regards assessment of the general first-order form of equation (A1), rather than its detailed quantitative properties. Equation (A1) indicates that a suitable first-order form for $\sigma_{Q,U}$ may be defined by

$$\sigma_{Q,U}^2 \equiv A_Q \hat{\sigma}_Q^2 + A_U \hat{\sigma}_U^2, \quad (\text{A2})$$

with positive factors A_Q and A_U satisfying $A_Q + A_U = 1$, and where these factors may be assumed to be constants (i.e. independent of Q_0 and U_0) to ensure that $\sigma_{Q,U}$ remains signal-independent (note comments at the end of § 2). To investigate whether the use of equation (A2), or the average standard error definition further above, could enable outliers within empirically-obtained $\sigma_Q \neq \sigma_U$ distributions to be suitably characterised by the analytic distributions for L and L_{RM} , we performed the following simulations.

We populated discrete distributions of $L/\sigma_{Q,U}$ (dimensionless) for $1 \leq \sigma_Q/\sigma_U \leq 1.5$ and examined how closely outliers beyond $\sim 5\sigma$ were fit by equation (11). Three definitions for $\sigma_{Q,U}$ were tested: $0.5(\hat{\sigma}_Q + \hat{\sigma}_U)$, equation (A2) with $A_Q = A_U = 0.5$, and a case where A_Q and A_U were varied in search of optimal values. We set up our simulations in two ways. In the first setup, we assumed that the variance in standard error estimates was zero, namely that $\hat{\sigma}_Q = \sigma_Q$ and $\hat{\sigma}_U = \sigma_U$. We found that selecting $A_Q = 1$ or $A_U = 1$ over- or underestimated the noise required to correctly model true outlier populations, respectively. Selecting these values in turn under- or overestimated the true statistical significance of outliers, respectively. We therefore note that if we conservatively defined $\sigma_{Q,U} \equiv \max(\sigma_Q, \sigma_U)$, then the statistical significance of outliers, as well as that of true polarized sources, would never be overestimated (though they would certainly be underestimated). To limit the degree to which the significance of polarization detections (both signal and noise) could be underestimated, whilst still generally preventing them from being overestimated, we found the following empirical values to be suitable for use in equation (A2):

$$A_Q = \begin{cases} 0.8 & \text{if } \sigma_Q \geq \sigma_U \\ 0.2 & \text{if } \sigma_Q < \sigma_U, \end{cases} \quad (\text{A3})$$

with $A_U = 1 - A_Q$. We found that use of these factors limited systematic underestimation of the statistical significance of $G^{ES} \approx 5\sigma$ outlier samples to $\lesssim 2\%$ of their true, empirically determined values; this underestimation peaked at $\sigma_Q/\sigma_U \sim 1.2$, diminishing elsewhere within the $1 \leq \sigma_Q/\sigma_U \leq 1.5$ range tested. For comparison, we found that the conservative definition $\sigma_{Q,U} \equiv \max(\sigma_Q, \sigma_U)$ performed worse, typically underestimating true significance values systematically by $\sim 6\%$. In the second simulation setup, we investigated the effects of uncertainties in $\hat{\sigma}_Q$ and $\hat{\sigma}_U$ by assuming what we envisaged to be \sim worst-case 10% errors in each. The factors from equation (A3) were again found to be suitable in these simulations.

The results of our L simulations are summarised in Fig. A1 for the three $\sigma_{Q,U}$ definitions tested, and for three noise cases: $\sigma_Q = \sigma_U$, $\sigma_Q = 1.1\sigma_U$, and $\sigma_Q = 1.5\sigma_U$. We found that introducing variance into the standard error es-

timates affected the empirical L distributions in a manner similar to the influence of introducing $\sigma_Q \neq \sigma_U$, shifting outlier populations away from the analytic PDFs. We found that the $0.5(\hat{\sigma}_Q + \hat{\sigma}_U)$ and $A_Q = A_U = 0.5$ definitions for $\sigma_{Q,U}$ resulted in empirical distributions that were closely fit by equation (11) at low-SNRs, but which resulted in increasingly poor fits for outlier populations as either variance was introduced to the standard error estimates or $\sigma_Q \neq \sigma_U$ was introduced. The $A_Q = A_U = 0.5$ definition resulted in marginally improved fits for noise outliers compared with the average standard error definition. The third definition, using equation (A2) with factors from equation (A3), resulted in empirical distributions most accurately fit by equation (11) for outliers, though at the expense of poor fitting at low-SNR. We found that this definition of $\sigma_{Q,U}$ optimally accounted for unequal noise within the range tested, even when variance in standard error estimates was introduced (though less so towards the upper end of the range where $\sigma_Q/\sigma_U = 1.5$).

We performed similar simulations for L_{RM} to investigate suitability of the $\sigma_{Q,U}$ definitions considered above in this different statistical environment. We simplified the potential complexity of these simulations by assuming the following illustrative \sim worst-case setup based on the $M = 30$, 24 spectral channel setup described in § 3. Individual samples of L_{RM} were obtained empirically by selecting the maximum of $M = 30$ independent Rayleigh-distributed variates. Each of these variates was assumed to represent a uniformly-weighted stack of 24 spectral channels, namely with equation (21) set to unity. We investigated unequal noise by systematically assuming $\sigma_{Q,i} = \sigma_{U,i}$, $\sigma_{Q,i} = 1.1\sigma_{U,i}$, or $\sigma_{Q,i} = 1.5\sigma_{U,i}$ for each i 'th channel, and investigated the influence of uncertainties in estimates of standard error by introducing 10% error to $\hat{\sigma}_{Q,i}$ and $\hat{\sigma}_{U,i}$ for each channel (thus $10/\sqrt{24}\%$ in each of the 30×2 stacked Q and U values used to obtain each sample of L_{RM}).

The results of our L_{RM} simulations are displayed in Fig. A2. We found similar behaviour of the different $\sigma_{Q,U}$ definitions to that exhibited in Fig. A1. However, the effect of introducing unequal noise was found to be more prominent within outlier populations in Fig. A2 due to their being selected from a maximum of $M = 30$ samples. This effect will be further pronounced for data with larger M , though because it is unlikely that all spectral channels will exhibit the systematic unequal noise assumed in our worst-case simulations, the outlier populations in real data are unlikely to be as extreme as those presented here. Additionally, if channel weighting is introduced according to equation (21), the impacts of bad channel data will be minimised and outlier populations further reduced. Regarding the introduction of variance in $\hat{\sigma}_{Q,i}$ and $\hat{\sigma}_{U,i}$, we note that its impact on outlier populations will be minimised for data with a greater number of spectral channels, due to the $1/\sqrt{T}$ dependence in stacked channel data. As with the simulations for L , we found that by defining $\sigma_{Q,U}$ using equation (A2) with the factors from equation (A3), outlier populations of the various empirical distributions investigated were aligned robustly with the analytic distribution given by equation (25).

We conclude that the analytic equations presented in the main body of this paper may be utilised for data exhibiting modest unequal noise of $\sim 10\%$, without incurring significant biases, by defining $\sigma_{Q,U}$ according to equation (A2)

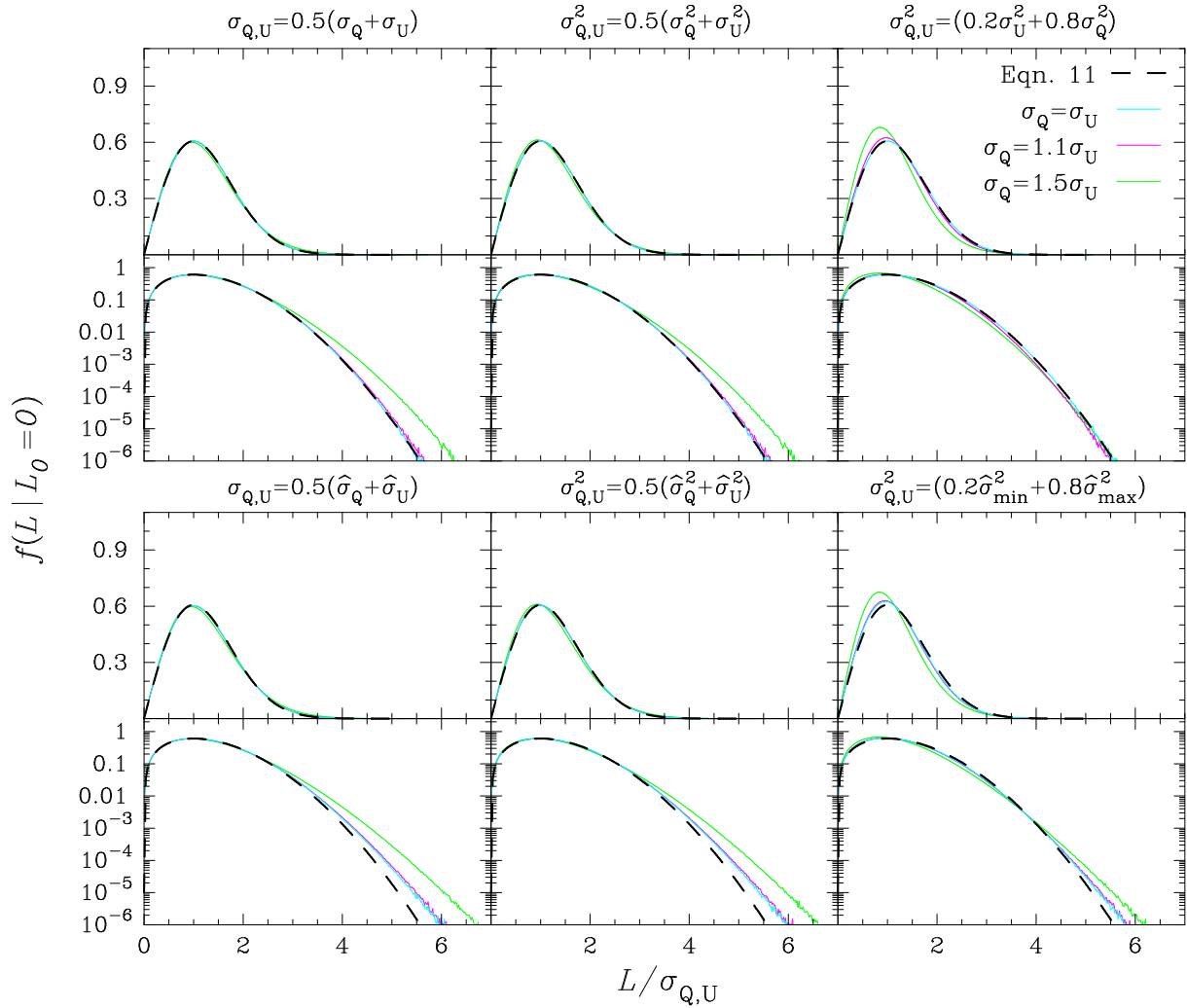


Figure A1. Empirical PDFs for L obtained for three noise cases (coloured curves), in which each L sample was normalised by $\sigma_{Q,U}$ in accordance with the three definitions indicated above the columns. For comparison, the analytic PDF for L given by equation (11) is presented identically in each panel; it is not fit to the data. Data from panels in the first and third rows are displayed with logarithmic scaling in the second and fourth rows, respectively. The upper set of panels are for the simulations with known standard errors, namely for $\hat{\sigma}_Q = \sigma_Q$ and $\hat{\sigma}_U = \sigma_U$. The lower set of panels are for the simulations with 10% errors in $\hat{\sigma}_Q$ and $\hat{\sigma}_U$. Small-number statistics begin to cause artificial broadening of the empirical distributions below densities of $\sim 10^{-5}$.

with factors from equation (A3). While our simulations have indicated that this definition may be suitable for data exhibiting more extreme unequal noise, we caution that we have not considered the potential impacts of biases on polarization position angles; future investigation regarding this issue is clearly required.

This paper has been typeset from a $\text{\TeX}/\text{\LaTeX}$ file prepared by the author.

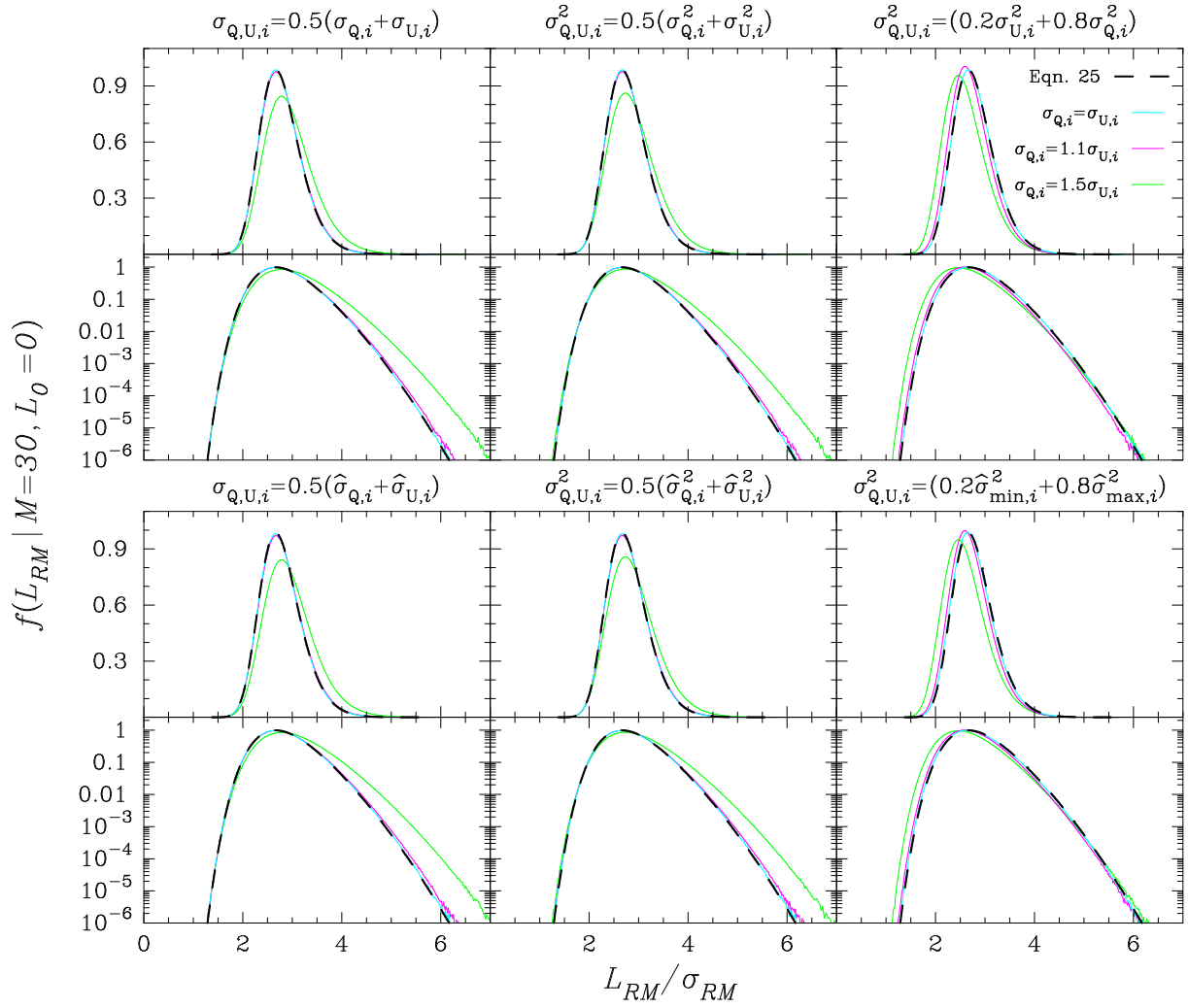


Figure A2. Empirical PDFs for L_{RM} compared with the analytic PDF given by equation (25); see text for details. The layout follows that described for Fig. A1.